AIAA AVIATION Forum
17-21 June 2019, Dallas, Texas
AIAA Aviation 2019 Forum

10.2514/6.2019-3338

High-Order Numerical Simulation of Flapping Wing for Energy Harvesting

Bin Zhang* and Chunlei Liang†
The George Washington University, Washington, DC 20052, USA

The energy harvesting performances of an isolated flapping wing and a tandem-flapping-wing system are numerically studied using a high-order flux reconstruction method with sliding meshes. It is found that, even at a moderate Reynolds number, viscous force has negligible contribution to energy harvesting, while pressure has dominant effects. Meanwhile, heaving motion is noticed to play a more vital role in energy harvesting than pitching motion. Through flow field visualization, it is also observed that the effective angle of attack greatly alters leading edge and trailing edge vortices and in turn affects energy harvesting. The tandem-wing simulation reveals that, when well positioned, the system exhibits higher energy efficiency than an isolated wing under the same flow conditions.

I. Introduction

FLAPPING wing has two working regimes: thrust generation when pitching motion proceeds heaving motion [1], and energy harvesting when heaving proceeds pitching [2]. In recent years, the increasing demands on renewable energy have drawn a wide range of interests in the latter regime.

McKinney and DeLaurier [2] built the first flapping-wing windmill for energy harvesting and studied the performance theoretically and experimentally. They pointed out that a wing achieves the maximum energy extraction efficiency when its heaving motion proceeds pitching motion for 90 degrees in phase. Jones et al. [3] performed panel method simulation and water tank experiment of a flapping wing which they called "flutter engine". Their simulation showed reasonable agreement with the experiments of McKinney and DeLaurier [2]. They also investigated the effects of plunging and obtained optimal values for their setup.

More recently, Kinsey and Dumas [4] numerically studied a flapping NACA0015 airfoil, in which they fixed the heaving amplitude and phase, and varied the reduced frequency and pitching amplitude. Their work revealed that the efficiency can be improved by more than 20% when pitching amplitude is above 55°. Ashraf et al. [5] studied a flapping NACA0014 airfoil at Reynolds number 20,000. They reported that better efficiency can be achieved using a non-sinusoidal motion profile. Kinsey and Dumas [6] also simulated tandem flapping wings at Reynolds number 500,000 using unsteady RANS. They noticed that the trailing wing generally extracts less energy than the leading wing, and suggested that the efficiency can be improved by increasing pitching amplitude of the trailing wing. More recent research progress on this topic can be found in, for example, the review paper by Young et al. [7].

Numerical simulation of flapping wing faces two major challenges. One is the excessive mesh deformation due to large pitching and heaving motions. The other is numerical dissipation which is detrimental to vortical flow structures that are known to have great effects on wing performance. The authors of the present work recently developed a high-order sliding-mesh method [8–10] for the spectral difference (SD) method and the flux reconstruction (FR) method, which is suitable for studying flapping wing problem. The SD method was first introduced by David Kopriva [11–13] on quadrilateral grids for solving the Euler equations and the Navier-Stokes equations. Liu et al. [14], Wang et al. [15] and May and Schöberl [16] extended this method to unstructured triangular grids. The SD method solves equations in differential form directly, and solutions are approximated by discontinuous polynomials. This method has been shown to be high-order accurate and computationally efficient. We see a lot of extensions and applications of this method in recent years,

*Postdoctoral Scientist in the Department of Mechanical and Aerospace Engineering, email: bzh@gwu.edu
†Associate Professor in the Department of Mechanical and Aerospace Engineering, AIAA Associate Fellow

for example, in [17–21]. The FR method was developed more recently [22–28]. It shares a lot of similarities with the SD method, but at the same time shows distinct advantages. For example, numerical studies show that the FR method is more efficient than the SD method on both static and dynamic meshes [29, 30]; the FR method can recover many existing methods and can even produce new schemes that were never reported before.

In the present work, we apply our sliding-mesh method [8–10] with the FR method to study flapping wings for energy harvesting. In our method, we decompose a computational domain into sliding and deforming regions. In this way, heaving and pitching motions of a wing are easily decoupled, and good mesh qualities are maintained through out a simulation. Meanwhile, the high-order accuracy of the methods helps reduce numerical dissipations dramatically to ensure high-fidelity results.

This paper is organized as follows. In Section II, we give detailed description of the problem and the related terminology definitions. In Section III, we briefly introduce the numerical methods. Simulation results of an isolated flapping wing are reported in Section IV. A tandem wing system is then studied in Section V. Finally, Section VI concludes this paper.

II. Problem Definition

II.A. Wing Motion

In the present study, we use sinusoidal profiles as the heaving and pitching motions of a flapping wing. The mathematical expressions are

$$h(t) = h_0 \sin(2\pi f t + \phi), \tag{1}$$

$$\theta(t) = \theta_0 \sin(2\pi f t), \tag{2}$$

where $h(t)$ is the instantaneous heaving displacement, $\theta(t)$ is the instantaneous pitching angle, h_0 and θ_0 are the heaving and the pitching amplitudes, f is the frequency, and ϕ is the phase angle. Note that, the heaving displacement is measured from wing center to the mean position, and we assume that the wing center is at one third chord. The pitching angle is measured between chord and the freestream direction. As an example, Fig. 1 shows a schematic of the motion of an isolated wing in one period, where the phase angle is $\phi = 90°$.

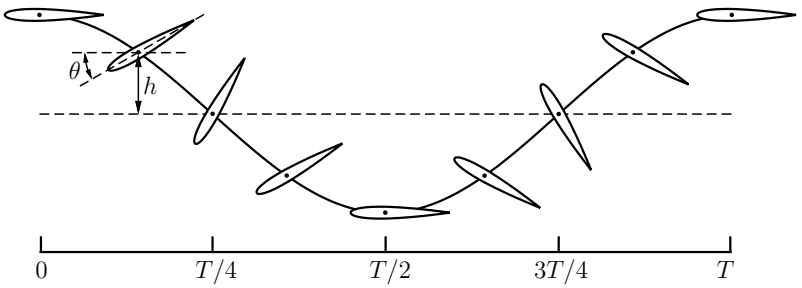

Figure 1. Schematic of an isolated flapping wing with $\phi = 90°$ in one period.

For two tandem flapping wings, we assume that the two wings are separated by a distance of L (measured from wing center to wing center in the streamwise direction). For simplicity, we further limit the difference of the two wings to a phase angle Φ between them. Their motions can be written as

$$h_1(t) = h_0 \sin(2\pi f t + \phi), \quad h_2(t) = h_0 \sin(2\pi f t + \Phi + \phi), \tag{3}$$

$$\theta_1(t) = \theta_0 \sin(2\pi f t), \qquad \theta_2(t) = \theta_0 \sin(2\pi f t + \Phi). \tag{4}$$

Here, the subscripts '1' and '2' represent the leading and the trailing wing, respectively. The rest variables have the same meanings as those for an isolated wing. For convenience, we call Φ the wing angle. Fig. 2 shows a schematic of a two-tandem wing system in one period, where the wing angle is $\Phi = -90°$ and the motion phase angle is $\phi = 90°$.

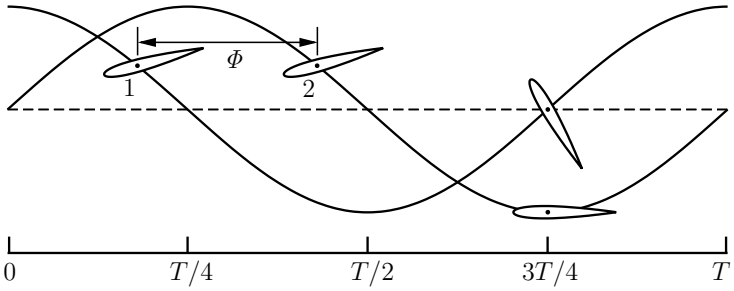

Figure 2. Schematic of two tandem wings with $\Phi = -90^\circ$ and $\phi = 90^\circ$ in one period.

II.B. Performance Measurements

Heaving and pithing both contribute to the overall energy harvesting of a wing. The instantaneous power from these two motions are

$$P_h(t) = Y\dot{h}(t), \quad P_\theta(t) = M\dot{\theta}(t), \tag{5}$$

where Y is the vertical force on a wing, $\dot{h}(t)$ is the heaving speed, M is the torque about wing center, and $\dot{\theta}(t)$ the angular speed. The total power is simply the sum of these two components, i.e.,

$$P(t) = P_h(t) + P_\theta(t). \tag{6}$$

There are a few factors that could affect a wing's energy harvesting performance. For example, the wing's configuration (such as heaving/pitching amplitude), fluid density, flow speed, etc. To isolate the effects of a wing's configuration, we introduce a nondimensional variable called coefficient of power that is defined as

$$C_P(t) \equiv \frac{P(t)}{\frac{1}{2}\rho_\infty U_\infty^3 c} = \frac{P_h(t)}{\frac{1}{2}\rho_\infty U_\infty^3 c} + \frac{P_\theta(t)}{\frac{1}{2}\rho_\infty U_\infty^3 c} = C_{P,h}(t) + C_{P,\theta}(t), \tag{7}$$

where ρ_∞ and U_∞ are the free-stream density and flow speed, c is the chord length, $C_{P,h}$ and $C_{P,\theta}$ are the heaving and the pitching power coefficients. Meanwhile, the force and torque on a wing come from two sources: pressure and viscosity. Therefore, we can also decompose the power coefficient into pressure and viscosity components to study their individual effects,

$$C_P(t) \equiv \frac{P(t)}{\frac{1}{2}\rho_\infty U_\infty^3 c} = \frac{P_{prs}(t)}{\frac{1}{2}\rho_\infty U_\infty^3 c} + \frac{P_{vis}(t)}{\frac{1}{2}\rho_\infty U_\infty^3 c} = C_{P,prs}(t) + C_{P,vis}(t), \tag{8}$$

where the subscripts 'prs' and 'vis' stand for pressure and viscosity, respectively.

The mean power coefficient is defined as the instantaneous power coefficient time-averaged over one motion period, that is

$$\overline{C}_P \equiv \frac{1}{T}\int_0^T C_P \mathrm{d}t = \frac{1}{T}\int_0^T C_{P,h}\mathrm{d}t + \frac{1}{T}\int_0^T C_{P,\theta}\mathrm{d}t = \overline{C}_{P,h} + \overline{C}_{P,\theta}, \tag{9}$$

where T is the period, $\overline{C}_{P,h}$ and $\overline{C}_{P,\theta}$ are the mean heaving and pitching power coefficients. Similarly, the mean power coefficients can also be written as

$$\overline{C}_P \equiv \frac{1}{T}\int_0^T C_P \mathrm{d}t = \frac{1}{T}\int_0^T C_{P,prs}\mathrm{d}t + \frac{1}{T}\int_0^T C_{P,vis}\mathrm{d}t = \overline{C}_{P,prs} + \overline{C}_{P,vis}, \tag{10}$$

where $\overline{C}_{P,prs}$ and $\overline{C}_{P,vis}$ are the mean pressure and viscosity power coefficients.

Finally, the energy harvesting efficiency, denoted by η, is defined as the ratio between the total energy harvested in a period and the total fluid kinematic energy passing through a wing's swept area in that time:

$$\eta \equiv \frac{\int_0^T P(t)\mathrm{d}t}{(\frac{1}{2}\rho_\infty U_\infty^2)\cdot d\cdot(U_\infty T)} = \frac{1}{T}\int_0^T \frac{P(t)}{\frac{1}{2}\rho_\infty U_\infty^3 c}\mathrm{d}t\cdot\frac{c}{d} = \frac{1}{T}\int_0^T C_P\mathrm{d}t\cdot\frac{c}{d} = \overline{C}_P\cdot\frac{c}{d}, \tag{11}$$

where d is the wing's swept area, which is usually larger than $2h_0$ due to tilting of the trailing and leading edges; all other variables, such as ρ_∞ and U_∞, have the same meanings as before.

III. Numerical Methods

This section gives a brief description of the flow equations and the numerical methods for solving them on sliding and moving grids, more details can be found in our previous papers [8–10].

III.A. Governing Equations

The flow in this study is governed by the two-dimensional Navier-Stokes equations, which has the following conservative form,

$$\frac{\partial \mathbf{Q}}{\partial t} + \frac{\partial \mathbf{F}}{\partial x} + \frac{\partial \mathbf{G}}{\partial y} = 0. \tag{12}$$

In the above equation, $\mathbf{Q}$ represents the vector of conservative variables, $\mathbf{F}$ and $\mathbf{G}$ the flux vectors. Their expressions are

$$\mathbf{Q} = [\rho\ \rho u\ \rho v\ E]^{\mathsf{T}}, \tag{13}$$

$$\mathbf{F} = \mathbf{F}_{inv}(\mathbf{Q}) + \mathbf{F}_{vis}(\mathbf{Q}, \nabla\mathbf{Q}), \tag{14}$$

$$\mathbf{G} = \mathbf{G}_{inv}(\mathbf{Q}) + \mathbf{G}_{vis}(\mathbf{Q}, \nabla\mathbf{Q}), \tag{15}$$

where ρ denotes density, u and v are the velocity components, E is the total energy per volume defined as

$$E = \frac{p}{\gamma - 1} + \frac{1}{2}\rho(u^2 + v^2), \tag{16}$$

and p is pressure, γ is the ratio of specific heats and is set to 1.4 here for ideal gas.

It is worth noting that, in Eqs. (14) and (15), the flux vectors have been decomposed into inviscid and viscous parts, which allows them to be treated separately. Their detailed expressions are

$$\mathbf{F}_{inv} = \begin{bmatrix} \rho u \\ \rho u^2 + p \\ \rho uv \\ (E+p)u \end{bmatrix},\ \mathbf{G}_{inv} = \begin{bmatrix} \rho v \\ \rho uv \\ \rho v^2 + p \\ (E+p)v \end{bmatrix}, \tag{17}$$

$$\mathbf{F}_{vis} = -\begin{bmatrix} 0 \\ \tau_{xx} \\ \tau_{yx} \\ u\tau_{xx} + v\tau_{yx} + \mathrm{k}T_x \end{bmatrix},\ \mathbf{G}_{vis} = -\begin{bmatrix} 0 \\ \tau_{xy} \\ \tau_{yy} \\ u\tau_{xy} + v\tau_{yy} + \mathrm{k}T_y \end{bmatrix}, \tag{18}$$

where $\tau_{ij} = \mu(u_{i,j} + u_{j,i}) + \lambda\delta_{ij}u_{k,k}$ is the shear stress tensor, μ is the dynamic viscosity, $\lambda = -2/3\mu$ based on the Stokes' hypothesis, δ_{ij} is the Kronecker delta, k is the thermal conductivity, T is temperature which is related to density and pressure through the ideal gas law: $p = \rho RT$, and R is the gas constant.

III.B. Computational Equations

To deal with moving grids, we employ an arbitrary Lagrangian-Eulerian (ALE) approach and transform a moving physical domain to a fixed computational one where computations are performed. Assume the physical time and space are (t, x, y), and the computational ones are (t, ξ, η), then it can be shown that the computational equations will take the following conservative form,

$$\frac{\partial \widetilde{\mathbf{Q}}}{\partial t} + \frac{\partial \widetilde{\mathbf{F}}}{\partial \xi} + \frac{\partial \widetilde{\mathbf{G}}}{\partial \eta} = 0, \tag{19}$$

and the computational variable and fluxes are related to the physical ones through

$$\begin{pmatrix} \widetilde{\mathbf{Q}} \\ \widetilde{\mathbf{F}} \\ \widetilde{\mathbf{G}} \end{pmatrix} = |\mathcal{J}|\mathcal{J}^{-1} \begin{pmatrix} \mathbf{Q} \\ \mathbf{F} \\ \mathbf{G} \end{pmatrix}, \tag{20}$$

where $|\mathcal{J}|$ is determinant of the Jacobian matrix, $\mathcal{J}^{-1}$ is the inverse Jacobian matrix, i.e.,

$$|\mathcal{J}| = \left|\frac{\partial(t,x,y)}{\partial(t,\xi,\eta)}\right| = \begin{vmatrix} 1 & 0 & 0 \\ x_t & x_\xi & x_\eta \\ y_t & y_\xi & y_\eta \end{vmatrix} = x_\xi y_\eta - x_\eta y_\xi, \tag{21}$$

$$\mathcal{J}^{-1} = \frac{\partial(t,\xi,\eta)}{\partial(t,x,y)} = \begin{bmatrix} 1 & 0 & 0 \\ \xi_t & \xi_x & \xi_y \\ \eta_t & \eta_x & \eta_y \end{bmatrix} = \frac{1}{|\mathcal{J}|}\begin{bmatrix} |\mathcal{J}| & 0 & 0 \\ -x_t y_\eta + y_t x_\eta & y_\eta & -x_\eta \\ x_t y_\xi - y_t x_\xi & -y_\xi & x_\xi \end{bmatrix}. \tag{22}$$

To ensure free-stream preservation on moving grids (i.e., a constant free-stream flow should always stay constant), the following geometric conservation laws (GCL) [31] also need to be satisfied numerically,

$$\begin{cases} \dfrac{\partial(|\mathcal{J}|\xi_x)}{\partial\xi} + \dfrac{\partial(|\mathcal{J}|\eta_x)}{\partial\eta} = 0, & (23) \\ \dfrac{\partial(|\mathcal{J}|\xi_y)}{\partial\xi} + \dfrac{\partial(|\mathcal{J}|\eta_y)}{\partial\eta} = 0, & (24) \\ \dfrac{\partial|\mathcal{J}|}{\partial t} + \dfrac{\partial(|\mathcal{J}|\xi_t)}{\partial\xi} + \dfrac{\partial(|\mathcal{J}|\eta_t)}{\partial\eta} = 0. & (25) \end{cases}$$

In this work, since grid motion is analytically given, and the spatial discretization is direct differentiation (will be discussed later), the first two GCL equations are automatically satisfied. From the last one, $|\mathcal{J}|$ is treated as an unknown, and is solved by using the same temporal and spatial discretization methods as those for the flow equations. This numerical $|\mathcal{J}|$ is then used to update the physical solutions.

III.C. Flux Reconstruction Method

In flux reconstruction (FR) method, each grid element is first mapped to a standard unit square element using, for instance, iso-parametric mapping. Then, solution points (SPs) and flux points (FPs) are defined in the interior and on the boundaries of a standard element, respectively. For an N-th order FR method, N SPs are defined in each coordinate direction, and N FPs are defined on each boundary edge. For example, Fig. 3 shows a schematic of the distribution of SPs and FPs for a fourth-order FR scheme.

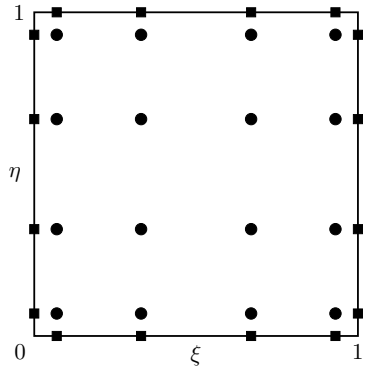

Figure 3. Schematic of solution points (circular dots) and flux points (square dots) for a fourth-order FR scheme.

Let X_s denote coordinate of an SP, then a Lagrange interpolation basis can be defined at the i-th SP,

$$h_i(X) = \prod_{s=1, s\neq i}^{N} \left(\frac{X - X_s}{X_i - X_s}\right), \tag{26}$$

which allows us to construct solution and flux polynomials using tensor products as

$$\widetilde{\mathbf{Q}}(\xi,\eta) = \sum_{j=1}^{N}\sum_{i=1}^{N} \widetilde{\mathbf{Q}}_{ij} h_i(\xi) h_j(\eta), \tag{27}$$

$$\widetilde{\mathbf{F}}(\xi,\eta) = \sum_{j=1}^{N}\sum_{i=1}^{N} \widetilde{\mathbf{F}}_{ij} h_i(\xi) h_j(\eta), \tag{28}$$

$$\widetilde{\mathbf{G}}(\xi,\eta) = \sum_{j=1}^{N}\sum_{i=1}^{N} \widetilde{\mathbf{G}}_{ij} h_i(\xi) h_j(\eta), \tag{29}$$

where $\widetilde{\mathbf{Q}}_{ij}$, $\widetilde{\mathbf{F}}_{ij}$ and $\widetilde{\mathbf{G}}_{ij}$ are the computational variable and fluxes at the (i,j)-th SP, respectively.

However, the above polynomials are only continuous within each element, but discontinuous across element boundaries. Therefore, common values need to be defined at cell boundaries. Here, the common solutions are calculated as the average of the left and the right values of a boundary. The common inviscid fluxes are computed using Riemann solver (for example, the Rusanov solver [32]). The common viscous fluxes are computed from common solutions and common gradients, where the common gradients are taken as the average of the left and the right values of a boundary.

Moreover, due to the first-order spatial derivatives on the flux terms, the flux polynomials need to be at least one degree higher than the solution polynomials in order to give the correct orders of accuracy. This is achieved by using correction functions. As an example, the corrected flux polynomial in the ξ direction is

$$\widetilde{\mathbf{F}}_c(\xi) = \widetilde{\mathbf{F}}(\xi) + (\widetilde{\mathbf{F}}_L^{com} - \widetilde{\mathbf{F}}_L)\cdot g_L(\xi) + (\widetilde{\mathbf{F}}_R^{com} - \widetilde{\mathbf{F}}_R)\cdot g_R(\xi), \tag{30}$$

where $\widetilde{\mathbf{F}}_L^{com}$ and $\widetilde{\mathbf{F}}_L$ are the common and the discontinuous fluxes at $\xi = 0$; $\widetilde{\mathbf{F}}_R^{com}$ and $\widetilde{\mathbf{F}}_R$ are values at $\xi = 1$; $g_L(\xi)$ and $g_R(\xi)$ are the left and the right correction functions. The correction functions are polynomials that are at least one-degree higher than the original flux polynomials. They must satisfy

$$g_L(0) = 1, \quad g_L(1) = 0, \quad g_R(0) = 0, \quad g_R(1) = 1, \tag{31}$$

to ensure continuity. In this work, we use the g_{DG} correction function [22, 23] for this purpose.

Finally, the computational equation is written in the following residual form

$$\frac{\partial \widetilde{\mathbf{Q}}}{\partial t} = -\frac{\partial \widetilde{\mathbf{F}}_c}{\partial \xi} - \frac{\partial \widetilde{\mathbf{G}}_c}{\partial \eta}, \tag{32}$$

and is time marched using a five-stage fourth-order strong stability preserving Runge-Kutta method [33, 34].

III.D. Mesh Movement Method

We take the schematic in Fig. 4 as an example to explain how we control mesh movements. The overall domain is split into two physical subdomains: an inner circular subdomain Ω_1 (with a radius R_s) that encloses the wing, and an outer one Ω_2 that takes the rest of the domain. Ω_2 is further divided into three virtual subdomains, i.e., $\Omega_{2,1}$, $\Omega_{2,2}$ and $\Omega_{2,3}$, by two virtual circles at R_a and R_b. We let mesh in Ω_1 and

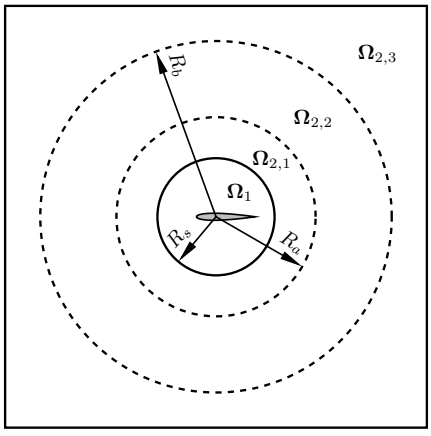

Figure 4. Schematic of sliding and deforming regions for a flapping wing simulation.

$\Omega_{2,1}$ translate (without deformation) following the wing's heaving motion. Meanwhile, Ω_1 rotates relative

to $\Omega_{2,1}$, forming a sliding interface in between. Then, we let mesh in $\Omega_{2,2}$ deform to accommodate the heaving motion of $\Omega_{2,1}$. Finally, mesh in $\Omega_{2,3}$ stays stationary all the time. The mesh deformation in $\Omega_{2,2}$ is controlled by a blending function. More details can be found in our previous paper [9].

To deal with the nonconforming sliding-mesh interface, we developed a curved dynamic mortar method [8, 9] and recently extended it to general nonuniform sliding meshes [10]. As an example, Fig. 5 shows a sliding mesh with two subdomains for a Taylor-Couette flow simulation. We employ virtual dynamic mortars, which are placed between the two subdomains, for communication. We first project discontinuous solutions

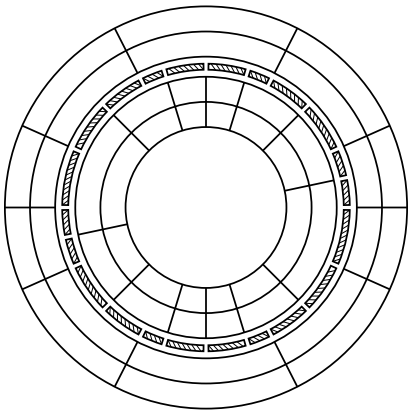

Figure 5. Schematic of the distribution of mortars (hatched) between a rotating mesh and a stationary mesh (inner domain has been scaled to show mortars in the middle).

from the two sides of a sliding interface to the two sides of the mortar elements. Then, common solutions and common fluxes are computed on the mortars. Finally, we project these common values from mortars back to subdomains to ensure continuity and conservation. This method maintains the high-order spatial and temporal accuracies of the SD and the FR methods, and is very efficient in terms of computational cost. It is also applicable to other problems, for example, simulation of vortex-induced vibrations [35].

IV. An Isolated Flapping Wing at Various ϕ's

The wing is chosen as a NACA0012 airfoil with a chord length $c = 1$. Its heaving and pitching amplitudes are $h_0 = 1$ and $\theta_0 = 75°$, respectively. The reduced frequency is $fc/U_\infty = 1/7$. The freestream flow has a Mach number $Ma_\infty = 0.1$, and Reynolds number $Re = \rho_\infty U_\infty c/\mu_\infty = 1000$. Fig. 6 shows the mesh for this study. The overall computational domain size is 100×100, and the distance between the wing and the inlet is 30. The whole domain is discretized into 8,313 quadrilateral mesh cells, with 437 of them inside a circular sliding region whose radius is 1. The 6^{th}-order FR scheme with a time step size of $\Delta t U_\infty/c = 1 \times 10^{-4}$

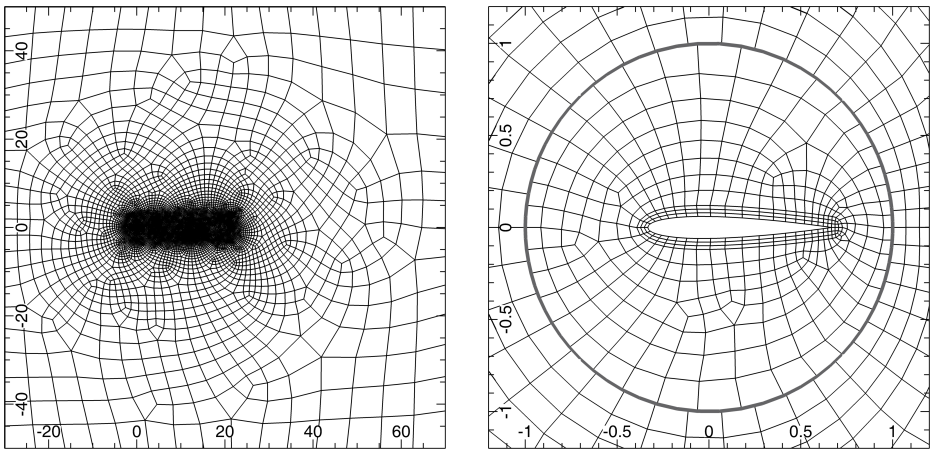

Figure 6. Global and local views of mesh for an isolated flapping wing (thick gray circle is sliding interface).

is used for the simulation. The wing surface is treated as adiabatic wall, and all other boundaries of the domain are set as characteristic far field. Seven phase angles ranging from 0° to 180° are studied. All the simulations were carried out for 300 time units (i.e., to $tU_\infty/c = 300$), and data from the last 20 flapping periods are used for post-processing. We have carefully checked all the solutions reported hereinafter to have made sure that they are well converged and are mesh-independent.

Fig. 7 shows time histories of the power coefficients for the seven cases. As we can see, all flows converge quickly, and all the converged flows look periodic. To further verify that the flows are indeed periodic before reporting other results, we have plotted in Fig. 8 the phase diagram of the lift coefficient (i.e., C_L) and the drag coefficient (i.e., C_D) for the last 20 flapping periods for all the cases. It is obvious that all curves repeat themselves very well, which confirms that all flows are very periodic.

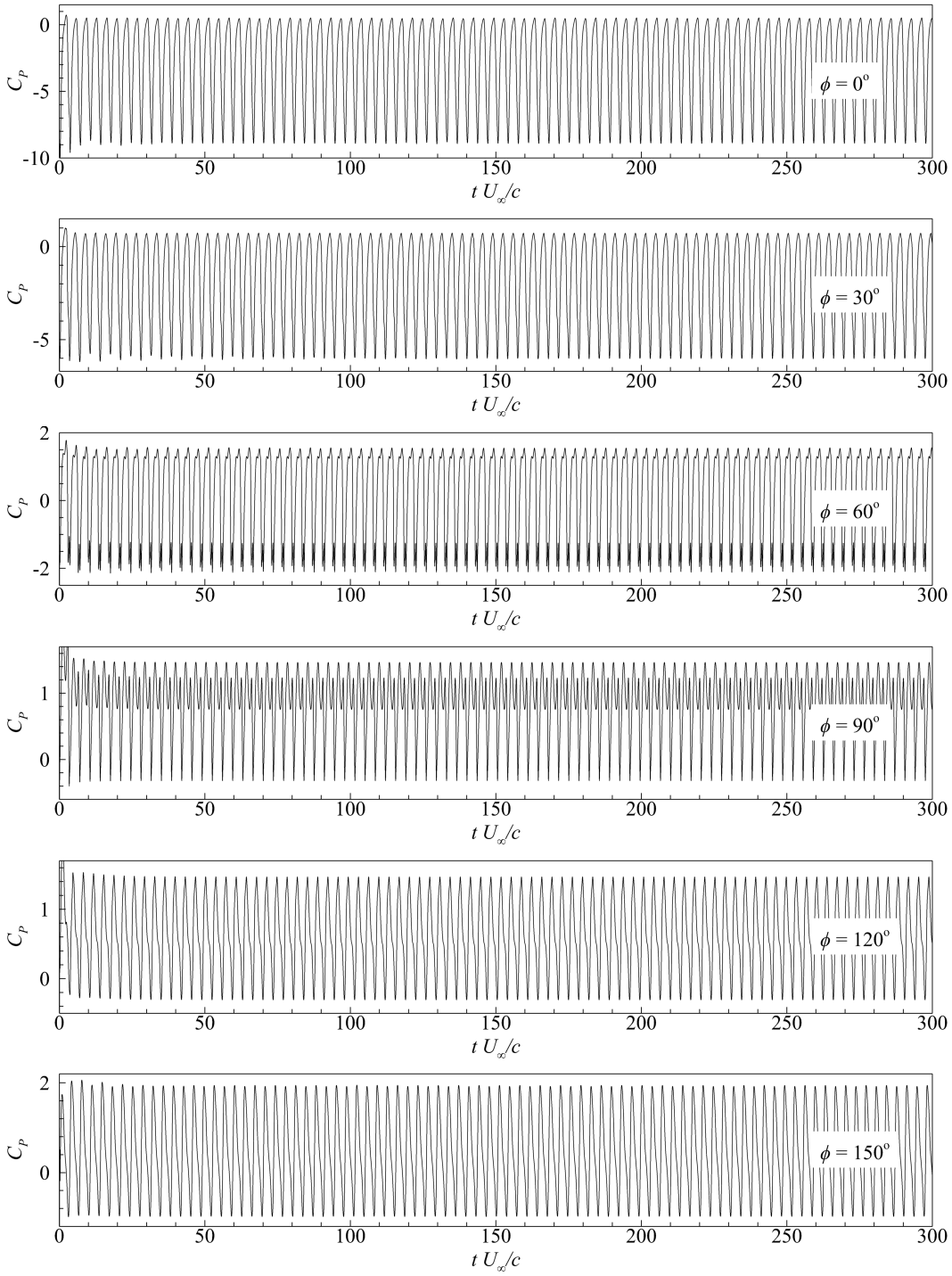

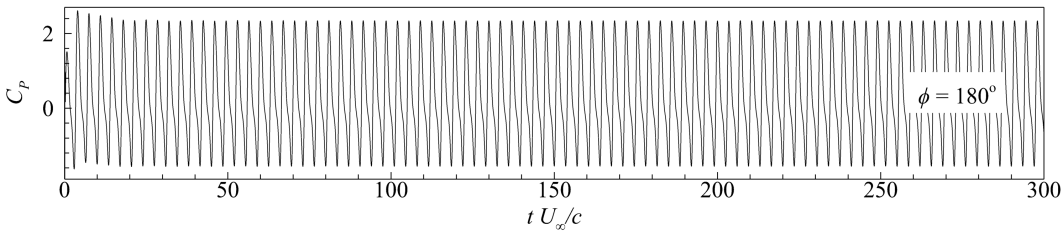

Figure 7. Time histories of power coefficients for an isolated flapping wing with various phase angles.

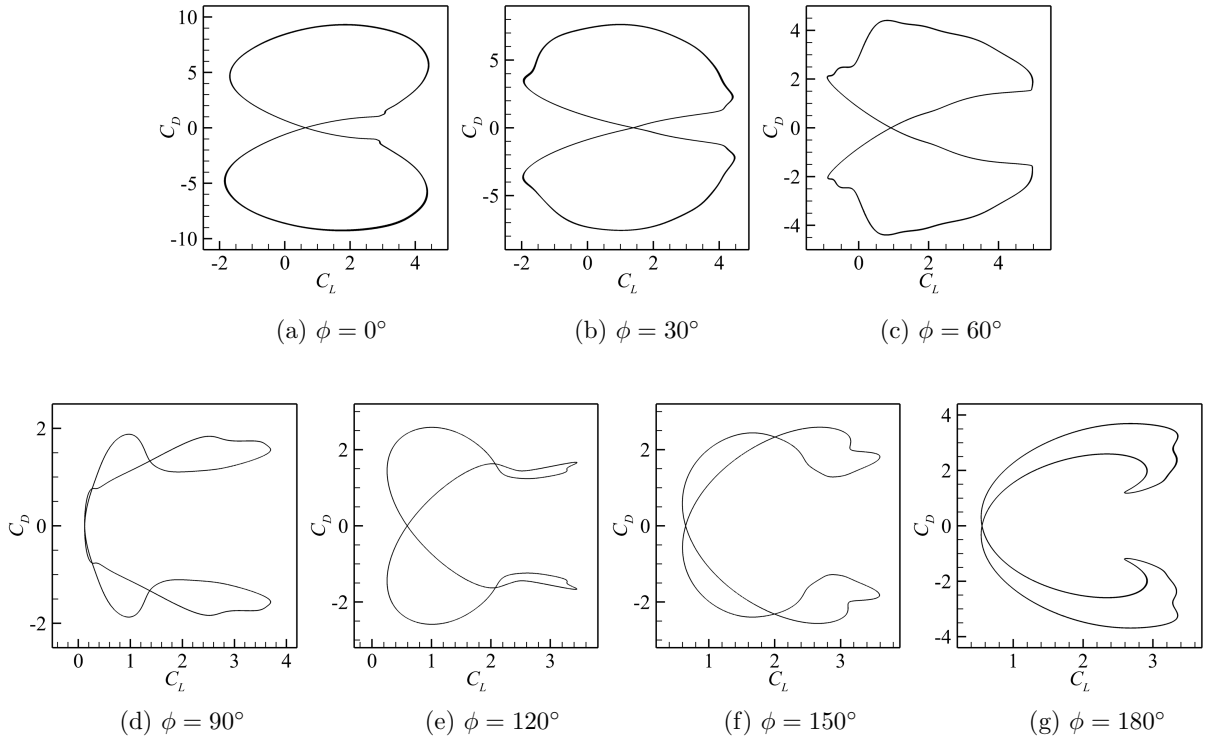

(a) $\phi = 0°$ (b) $\phi = 30°$ (c) $\phi = 60°$

(d) $\phi = 90°$ (e) $\phi = 120°$ (f) $\phi = 150°$ (g) $\phi = 180°$

Figure 8. Phase diagram of lift and drag coefficients for an isolated flapping wing in 20 flapping periods.

Fig. 9 shows the vorticity contours at $3T/4$, when the wing is at the maximum pitching angle. Two major differences are observed from the flow fields. The first difference is that, although all wings are at the same pitching angle, they have very different leading edge vortices (LEVs). For example, from $\phi = 0°$ to 180°, the sizes of the LEVs first decrease and then increase, with the smallest LEV found at $\phi = 90°$. This obviously has to do with the effective angle of attack (AOA), which is defined as below,

$$\alpha(t) = \arctan\left(-\dot{h}(t)/U_\infty\right) - \theta(t). \tag{33}$$

We have plotted the effective AOA in Fig. 10 for all the cases, and they are seen to have consistent trend with the LEVs. The second flow field difference lies in flow structures in the wake regions. For example, at $\phi = 90°$ and 120°, the wakes have an upper row of clockwise (negative) vortices and a lower row of counterclockwise (positive) vortices, which represent typical velocity deficit wakes and indicate that the wing has harvested energy (the two rows are separated at a larger vertical distance at $\phi = 120°$, which indicates less flow velocity deficit and less energy harvesting). In contrast, at $\phi = 0°$, the wake contains only a single row of vortices with alternative signs, where the positive ones are slightly above the negative ones. This indicates that the wake has possibly been accelerated (in other words, the wing has lost energy to the flow).

The instantaneous power coefficients and their components are plotted in Fig. 11 and Fig. 12, where the data has been phase averaged for 20 periods. It is noticed in all figures that C_P and all its components have a period of $T/2$. This is because that a wing has the same energy harvesting performance in a downstroke as in an upstroke. From Fig. 11, it is seen that C_P and $C_{P,h}$ have very consistent trend, which means that

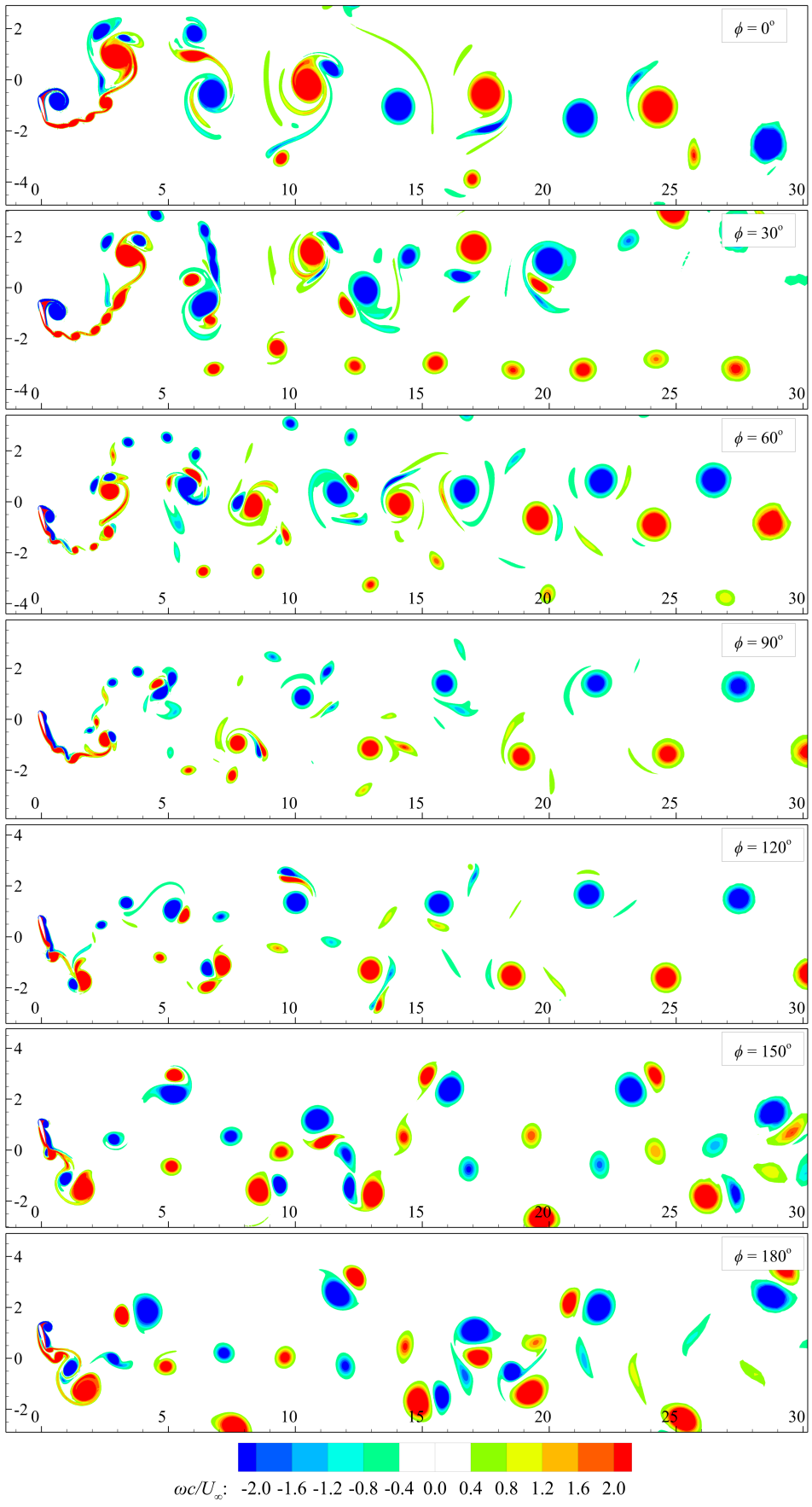

Figure 9. Vorticity contours at $3T/4$ for an isolated flapping wing with various phase angles.

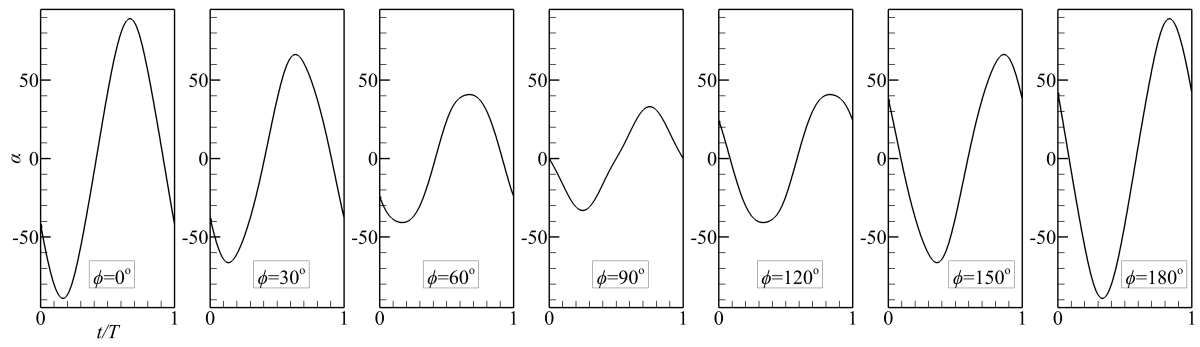

Figure 10. Effective angle of attack (in degrees) for an isolated flapping wing.

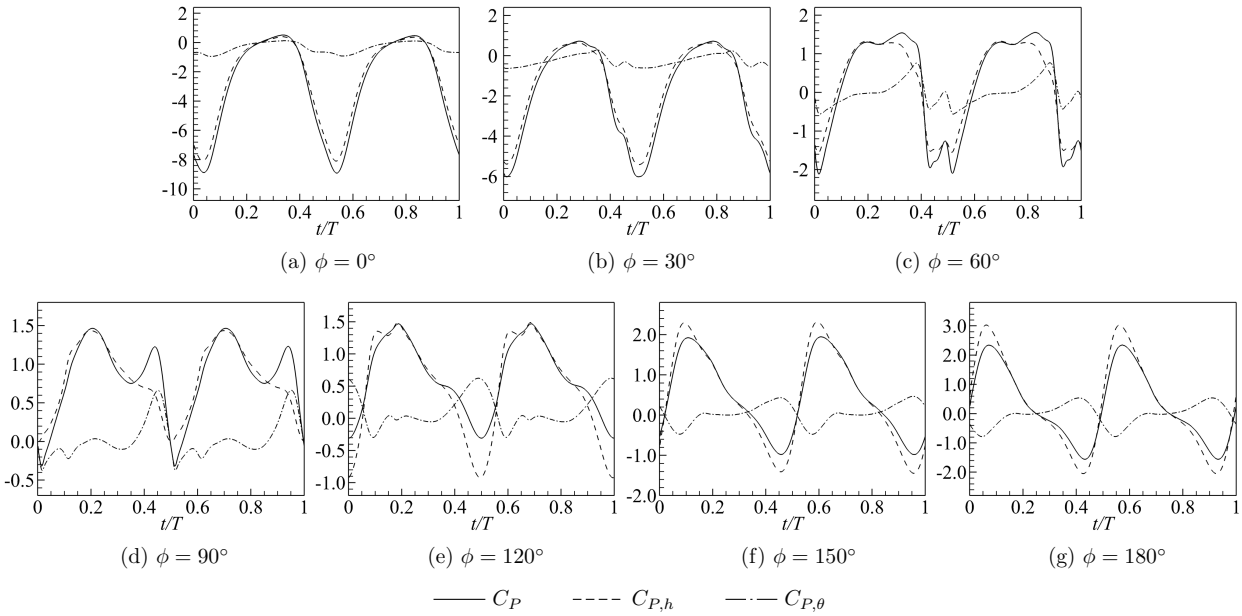

Figure 11. Power coefficient and its heaving and pitching components for an isolated flapping wing.

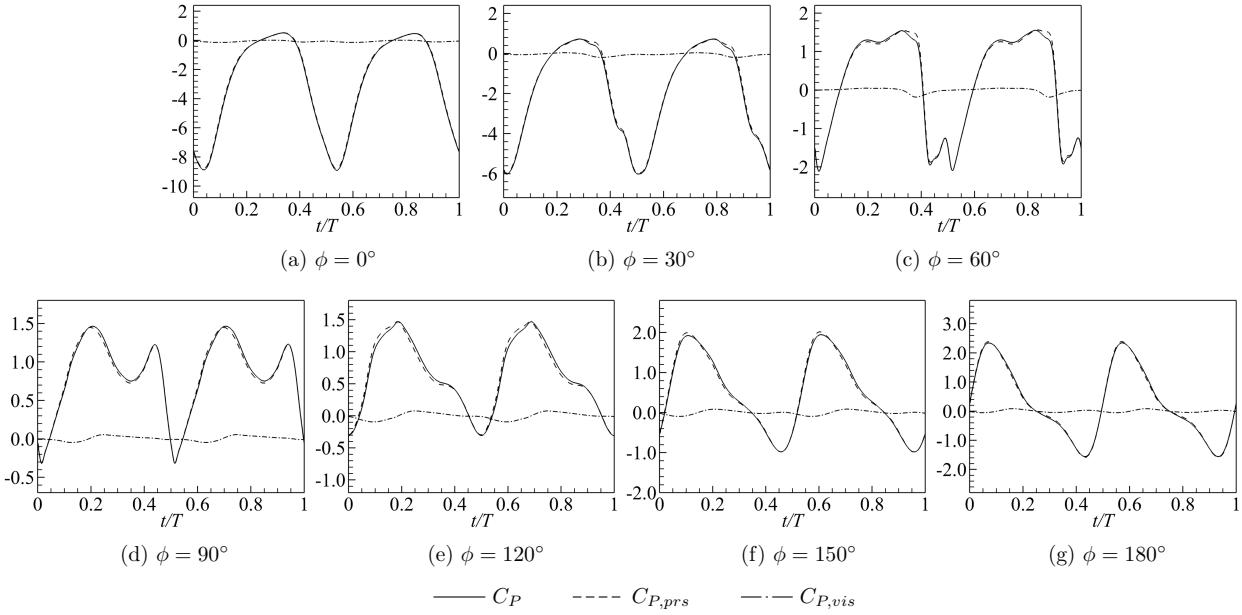

Figure 12. Power coefficient and its pressure and viscosity components for an isolated flapping wing.

energy harvesting is mostly dominated by the heaving motion (or the vertical force) but not the pitching motion (or the moment). However, the pitching angle does play an important role as it affects the effective AOA as indicated by Eq. (33). From the curves, we also see that, for all cases, the viscosity effects are negligibly small compared with the pressure contribution. Considering the moderate Reynolds number in this simulation (i.e., $Re = 1000$), it is very promising that potential flow can serve as a good approximation for this problem.

Finally, we report the mean power coefficients ($\overline{C}_P$) and the efficiencies (η) in Table 1. It is found that $\phi = 0°$ has the worst energy harvesting performance, as the wing loses a large amount of energy to the flow. In contrast, the best performance is found at $\phi = 90°$, which is consistent with the finding of McKinney and DeLaurier[2], and the wing harvests 32.8% (i.e., $\eta = 0.328$) of the fluid kinetic energy in the swept area. Qualitatively, these numbers agree with our previous observations from the flow fields in Fig. 9. Meanwhile, components of the mean power coefficient are also consistent with our previous conclusions from Fig. 11 and Fig. 12, i.e., heaving and pressure have dominant contributions to energy harvesting.

ϕ	$\overline{C}_P$	$\overline{C}_{P,h}$	$\overline{C}_{P,\theta}$	$\overline{C}_{P,prs}$	$\overline{C}_{P,vis}$	d/c	η
0°	-2.914	-2.567	-0.346	-2.847	-0.067	3.288	-0.886
30°	-1.841	-1.593	-0.248	-1.785	-0.056	3.230	-0.570
60°	0.219	0.238	-0.018	0.230	-0.011	3.004	0.073
90°	0.837	0.809	0.028	0.831	0.006	2.549	0.328
120°	0.636	0.513	0.123	0.639	-0.003	2.468	0.258
150°	0.488	0.446	0.042	0.489	-0.001	2.611	0.187
180°	0.295	0.326	-0.031	0.293	0.002	2.644	0.111

Table 1. Mean power coefficients and efficiencies of an isolated flapping wing with various phase angles.

V. Two Tandem Flapping Wings at Various Φ's

Fig. 13 shows two views of the mesh for this simulation. The overall domain has 9,857 cells, with 437 in each sliding subdomain whose radius is 1.0. Unless otherwise stated, all other simulation parameters such as the wing motion, the incoming flow condition, the Reynolds number, the boundary conditions, etc., are set the same as those for the isolated wing from Section IV. The wings here are separated by a distance $L/c = 7$, which is equivalent to an additional wing phase angle of 2π (because the wing's flapping period is 7). Both wings have $\phi = 90°$. Twelve wing angles ranging from $-180°$ to $180°$ are studied. However, it was found during post-processing that when $-180° < \Phi < 0°$, the trailing wing either loses energy to the flow or gains a very small amount of energy from the flow. For this reason, hereinafter we only report results for the seven cases with $0° \leq \Phi \leq 180°$.

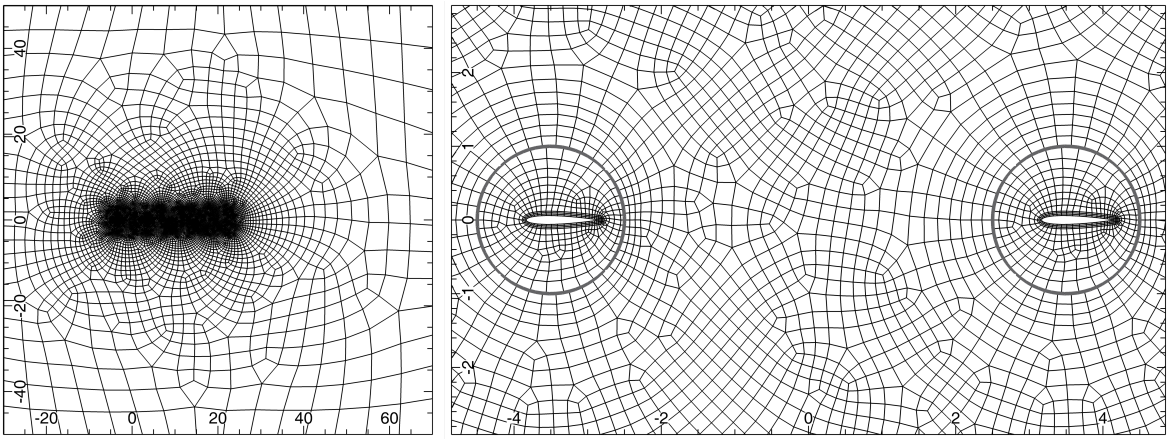

Figure 13. Global and local views of mesh for two tandem flapping wings (thick gray circles are sliding interfaces).

In Fig. 14, we plot the phase diagram of C_L and C_D for 20 flapping periods to check the flow periodicity,

where blue and red represent leading and trailing wings, respectively. As we can see, all flows, except the $\Phi = 0°$ case, exhibit very good periodicity. Meanwhile, the leading wing (in blue) is seen to experience almost identical forces in all cases, and they are close to those of the isolated wing with $\phi = 90°$.

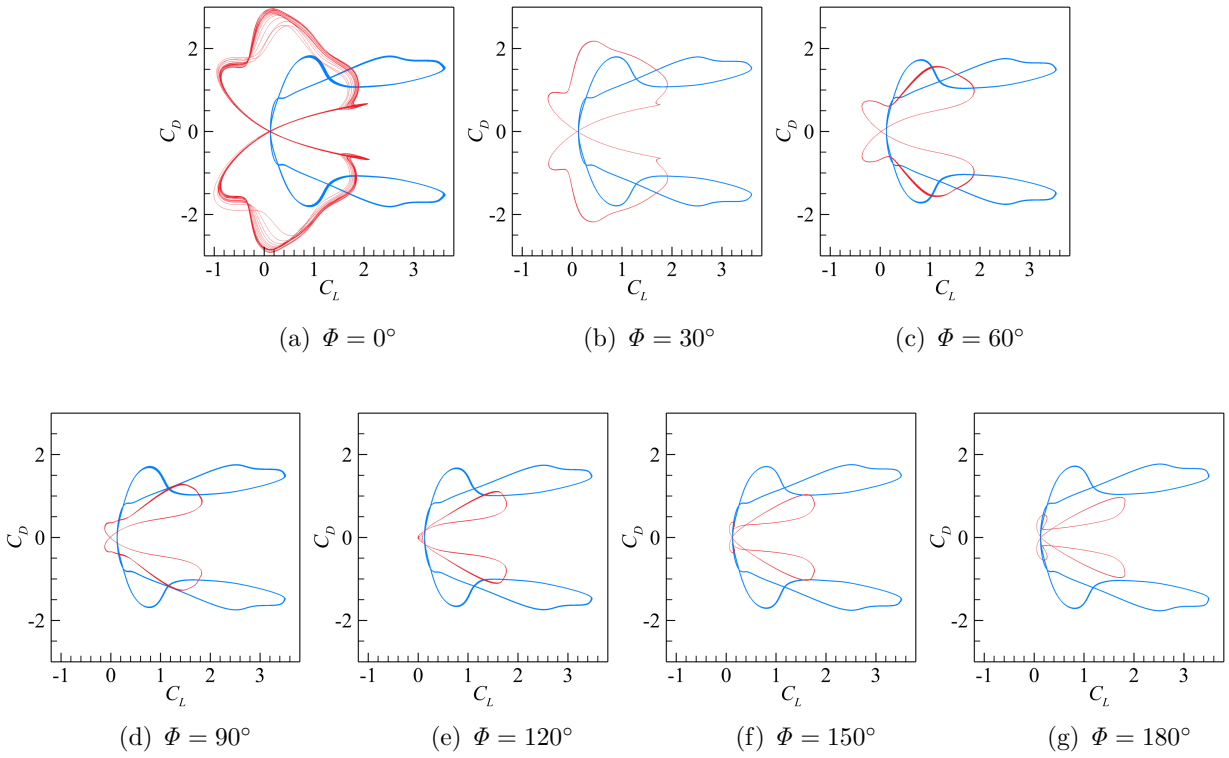

(a) $\Phi = 0°$ (b) $\Phi = 30°$ (c) $\Phi = 60°$

(d) $\Phi = 90°$ (e) $\Phi = 120°$ (f) $\Phi = 150°$ (g) $\Phi = 180°$

Figure 14. Phase diagram for two tandem flapping wings: blue, leading wing; red, trailing wing.

Fig. 15 shows the vorticity contours at $3T/4$ when the leading wing is at the maximum pithing angle. The flow fields look very different at a first glance. But a closer look reveals that each of them inevitably possesses a velocity deficit wake with an upper row of clockwise vortices and a lower row of counterclockwise vortices. At the same time, it is evident that the trailing wing has only minor effects on the leading wing, as the vortical flow structures around the leading wing are almost identical in all the cases. In fact, these vortical flow structures are even identical to those for the isolated wing with $\phi = 90°$ in Fig. 9. This is mainly because of the large distance between the two wings in the present setup. For this reason, we mainly focus on the performance of the trailing wing in what follows.

The phase averaged instantaneous power coefficient and its components for the tandem wing are shown in Fig. 16 and Fig. 17. Although the incoming flow conditions for the trailing wing are more complicated than that for the leading wing, the motion components and the force components are seen to have the same effects as those for an isolated wing: heaving and pressure play dominant roles, pitching almost always has negative contributions, and viscosity has negligible effects.

The mean power coefficients and efficiencies are reported in Table 2. We take the isolated wing with $\phi = 90°$ from Table 1 as a reference for comparison. By checking $\overline{C}_P$, it is obvious that for $0° \leq \Phi \leq 180°$, the tandem-wing system generally harvests more energy than the isolated wing. The maximum efficiency is found at $\Phi = 30°$, where the system harvests 40.5% (i.e., $\eta = 0.405$) fluid kinetic energy in the swept area and represents a relative 23.5% performance increase compared with the isolated wing. Furthermore, in this harvested energy, 78.1% comes from the leading wing (with $\overline{C}_{P1} = 0.808$), and only 21.9% comes from the trailing wing (with $\overline{C}_{P2} = 0.226$). The leading wing's performance is overall close to that of the isolated wing. A comparison between $\overline{C}_{P1}$ and $\overline{C}_{P2}$ reveals that the trailing wing generally extracts much less energy than the leading wing. One obvious reason is that the incoming flow for the trailing wing contains less kinetic energy than that for the leading wing (because the leading wing has already extracted a large amount of energy from the freestream flow). A comparison of $\overline{C}_{P2,h}$, $\overline{C}_{P2,\theta}$, $\overline{C}_{P2,prs}$ and $\overline{C}_{P2,vis}$ gives the same conclusion on their effects as from the instantaneous curves.

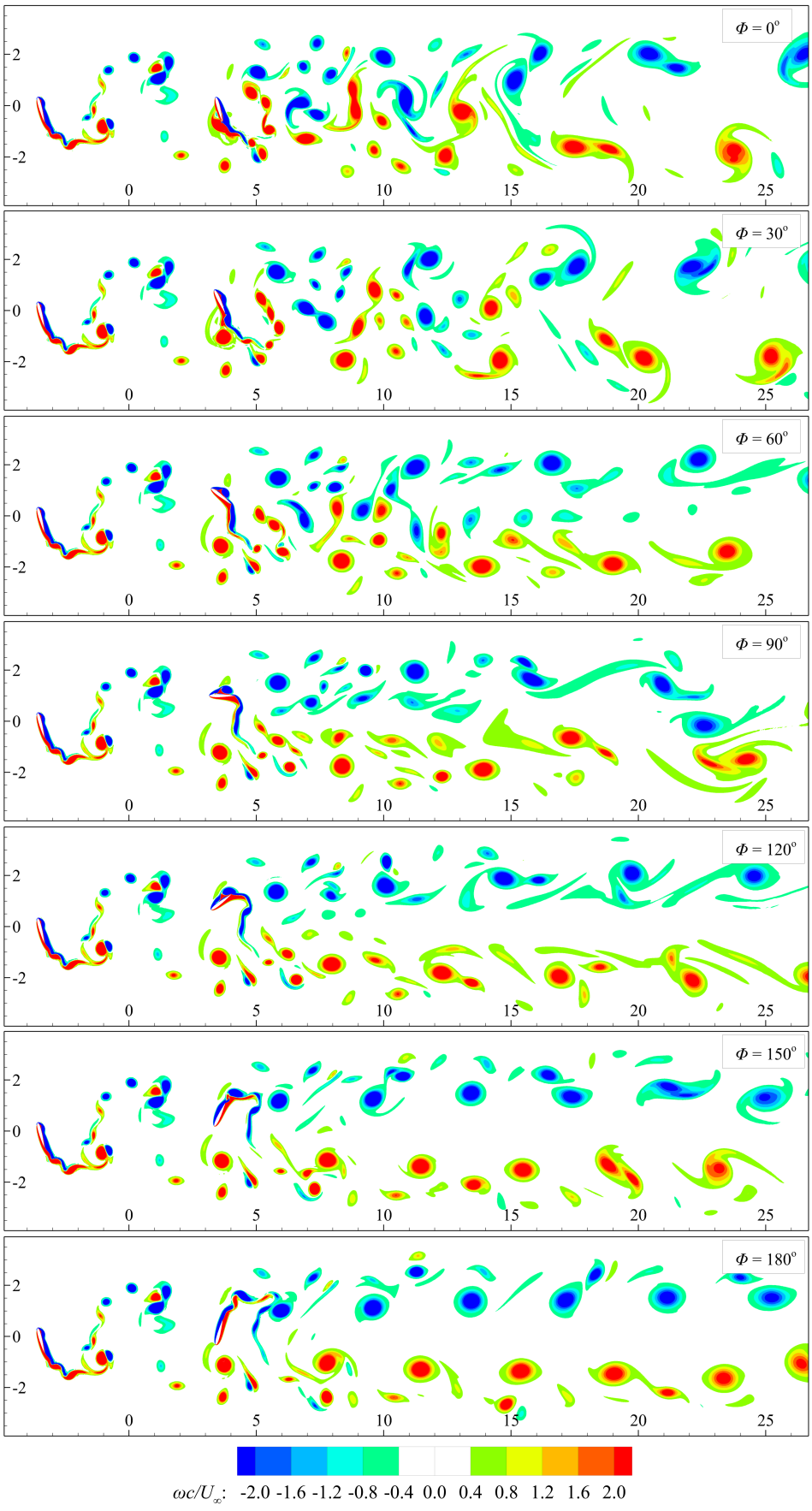

Figure 15. Vorticity contours for two tandem flapping wings at $3T/4$.

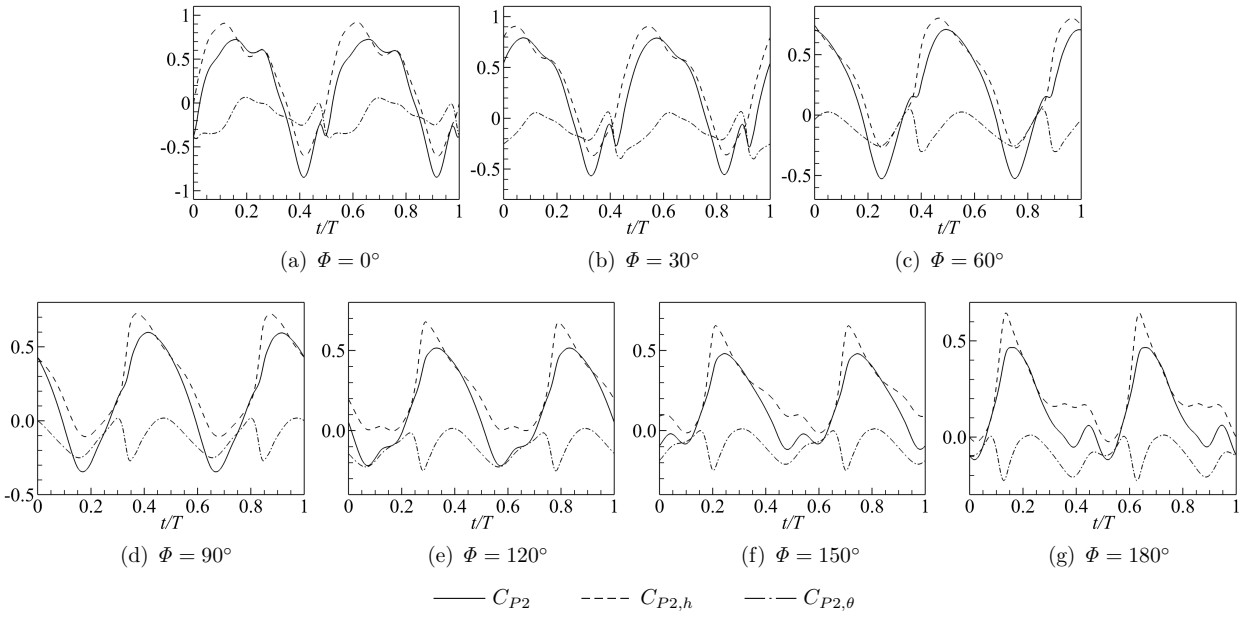

Figure 16. Power coefficient and its heaving and pitching components for the trailing flapping wing.

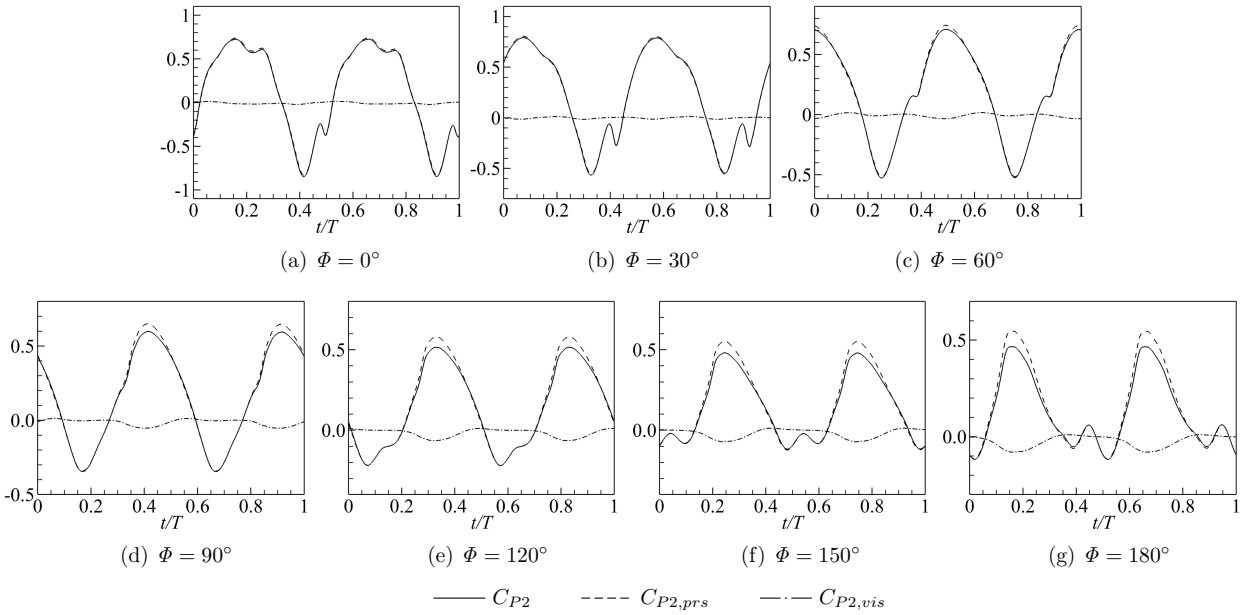

Figure 17. Power coefficient and its pressure and viscosity components for the trailing flapping wing.

Φ	$\overline{C}_P$	$\overline{C}_{P1}$	$\overline{C}_{P2}$	$\overline{C}_{P2,h}$	$\overline{C}_{P2,\theta}$	$\overline{C}_{P2,prs}$	$\overline{C}_{P2,vis}$	η	$\Delta\eta\%$
0°	0.957	0.815	0.142	0.297	-0.154	0.149	-0.007	0.375	14.3%
30°	1.034	0.808	0.226	0.351	-0.125	0.228	-0.002	0.405	23.5%
60°	0.974	0.781	0.193	0.309	-0.116	0.200	-0.007	0.382	16.5%
90°	0.933	0.771	0.162	0.274	-0.112	0.175	-0.013	0.366	11.6%
120°	0.908	0.763	0.145	0.250	-0.105	0.162	-0.017	0.356	8.5%
150°	0.922	0.774	0.148	0.242	-0.094	0.167	-0.020	0.361	10.1%
180°	0.913	0.780	0.133	0.223	-0.090	0.157	-0.025	0.358	9.1%

Table 2. Mean power coefficients and efficiency for two tandem flapping wings with various wing angles.

VI. Conclusions

We have applied our high-order sliding mesh flux reconstruction method to study energy harvesting of flapping wings. This method introduces minimum mesh distortion and minimum numerical dissipation by decoupling heaving and pitching motions through nonconforming sliding interfaces. A series of high fidelity simulation results are reported. From these results, we confirmed that an isolated wing harvests the most energy when heaving proceeds pitching for 90° in phase. From observation of the flow fields, it is noticed that the most efficient setup has the minimum effective angle of attack and the smallest leading edge vortex. Comparison of energy harvesting from the heaving and the pitching motions reveals that heaving plays a dominant role. Similarly, pressure effects are found to be much stronger than viscous effects at the given Reynolds number of 1000. In addition, simulation of a tandem-wing system shows that this system generally harvests more energy than an isolated wing when $0° \leq \Phi \leq 180°$, although the trailing wing is found to be less efficient than the leading wing. The optimum wing phase angle is found to be $\Phi = 30°$ for the current setup, where the system extract more than 40% of the fluid kinetic energy in the swept area. To further improve the performance of a tandem-wing system, a broader study involving more parameters, such as the separation distance L, heaving and pitching amplitudes, reduced frequency, ect., need to be carried out in the future.

References

[1] Shyy, W., Berg, M., and Ljungqvist, D., "Flapping and flexible wings for biological and micro air vehicles," *Progress in Aerospace Sciences*, Vol. 35, 1999, pp. 455–505.

[2] McKinney, W., and DeLaurier, J., "Wingmill: an oscillating-wing windmill," *Journal of Energy*, Vol. 5, 1981, pp. 109–115.

[3] Jones, K. D., Davids, S., and Platzer, M. F., "Oscillating-wing power generator," *Proceedings of the 3rd ASME/JSME Joint Fluids Engineering Conference*, 1999.

[4] Kinsey, T., and Dumas, G., "Parametric study of an oscillating airfoil in a power-extraction regime," *AIAA Journal*, Vol. 46, 2008, pp. 1318–1330.

[5] Ashraf, M. A., Young, J., Lai, J. C. S., and Platzer, M. F., "Numerical analysis of an oscillating-wing wind and hydropower generator," *AIAA Journal*, Vol. 49, 2011, pp. 1374–1386.

[6] Kinsey, T., and Dumas, G., "Optimal tandem configuration for oscillating-foils hydrokinetic turbine," *Journal of Fluids Engineering*, Vol. 134, 2012, p. 031103.

[7] Young, J., Lai, J. C. S., and Platzer, M. F., "A review of progress and challenges in flapping foil power generation," *Progress in Aerospace Sciences*, Vol. 67, 2014, pp. 2–28.

[8] Zhang, B., and Liang, C., "A simple, efficient, and high-order accurate curved sliding-mesh interface approach to spectral difference method on coupled rotating and stationary domains," *Journal of Computational Physics*, Vol. 295, 2015, pp. 147–160.

[9] Zhang, B., Liang, C., Yang, J., and Rong, Y., "A 2D parallel high-order sliding and deforming spectral difference method," *Computers & Fluids*, Vol. 139, 2016, pp. 184–196.

[10] Zhang, B., Qiu, Z., and Liang, C., "A flux reconstruction method with nonuniform sliding-mesh interfaces for simulating rotating flows," *AIAA paper 2018-1094*, 2018.

[11] Kopriva, D. A., and Kolias, J. H., "A conservative staggered-grid Chebyshev multidomain method for compressible flows," *Journal of Computational Physics*, Vol. 125, 1996, pp. 244–261.

[12] Kopriva, D. A., "A conservative staggered-grid Chebyshev multidomain method for compressible flows. II. A semi-structured method," *Journal of Computational Physics*, Vol. 128, 1996, pp. 475–488.

[13] Kopriva, D. A., "A staggered-grid multidomain spectral method for the compressible Navier-Stokes equations," *Journal of Computational Physics*, Vol. 143, 1998, pp. 125–158.

[14] Liu, Y., Vinokur, M., and Wang, Z. J., "Spectral difference method for unstructured grids I: Basic formulation," *Journal of Computational Physics*, Vol. 216, 2006, pp. 780–801.

[15] Wang, Z. J., Liu, Y., May, G., and Jameson, A., "Spectral difference method for unstructured grids II: Extension to the Euler equations," *Journal of Scientific Computing*, Vol. 32, 2007, pp. 45–71.

[16] May, G., and Schöberl, J., "Analysis of a spectral difference scheme with flux interpolation on raviart-thomas elements," *Aachen Institute for Advanced Study in Computational Engineering Science, Aachen*, 2010.

[17] Van den Abeele, K., Lacor, C., and Wang, Z. J., "On the stability and accuracy of the spectral difference method," *Journal of Scientific Computing*, Vol. 37, 2008, pp. 162–188.

[18] Jameson, A., "A proof of the stability of the spectral difference method for all orders of accuracy," *Journal of Scientific Computing*, Vol. 45, 2010, pp. 348–358.

[19] Liang, C., Jameson, A., and Wang, Z. J., "Spectral difference method for two-dimensional compressible flow on unstructured grids with mixed elements," *Journal of Computational Physics*, Vol. 228, 2009, pp. 2847–2858.

[20] Liang, C., Kannan, R., and Wang, Z. J., "A p-multigrid spectral difference method with explicit and implicit smoothers on unstructured triangular grids," *Computers & Fluids*, Vol. 38, 2009, pp. 254–265.

[21] Balan, A., May, G., and Schöberl, J., "A stable high-order spectral difference method for hyperbolic conservation laws on triangular elements," *Journal of Computational Physics*, Vol. 231, No. 5, 2012, pp. 2359–2375.

[22] Huynh, H. T., "A flux reconstruction approach to high-order schemes including discontinuous Galerkin methods," *AIAA paper 2007-4079*, 2007.

[23] Huynh, H. T., "A reconstruction approach to high-order schemes including discontinuous Galerkin for diffusion," *AIAA paper 2009-403*, 2009.

[24] Wang, Z. J., and Gao, H., "A unifying lifting collocation penalty formulation including the discontinuous Galerkin, spectral volume/difference methods for conservation laws on mixed grids," *Journal of Computational Physics*, Vol. 228, 2009, pp. 8161–8186.

[25] Vincent, P. E., Castonguay, P., and Jameson, A., "A new class of high-order energy stable flux reconstruction schemes," *Journal of Scientific Computing*, Vol. 47, 2011, pp. 50–72.

[26] Jameson, A., Vincent, P. E., and Castonguay, P., "On the non-linear stability of flux reconstruction schemes," *Journal of Scientific Computing*, Vol. 50, No. 2, 2012, pp. 434–445.

[27] Huynh, H. T., Wang, Z. J., and Vincent, P. E., "High-order methods for computational fluid dynamics: A brief review of compact differential formulations on unstructured grids," *Computers & Fluids*, Vol. 98, 2014, pp. 209–220.

[28] Wang, Z. J., and Huynh, H. T., "A review of flux reconstruction or correction procedure via reconstruction method for the Navier-Stokes equations," *Mechanical Engineering Reviews*, Vol. 3, No. 1, 2016.

[29] Liang, C., Cox, C., and Plesniak, M., "A comparison of computational efficiencies of spectral difference method and correction procedure via reconstruction," *Journal of Computational Physics*, Vol. 239, 2013, pp. 138–146.

[30] Liang, C., Miyaji, K., and Zhang, B., "An efficient correction procedure via reconstruction for simulation of viscous flow on moving and deforming domains," *Journal of Computational Physics*, Vol. 256, 2014, pp. 55–68.

[31] Thomas, P. D., and Lombard, C. K., "Geometric conservation law and its application to flow computations on moving grids," *AIAA Journal*, Vol. 17, 1979, pp. 1030–1037.

[32] Rusanov, V. V., "Calculation of interaction of non-steady shock waves with obstacles," *Journal of Computational and Mathematical Physics USSR*, Vol. 1, 1961, pp. 267–279.

[33] Kraaijevanger, J. F. B. M., "Contractivity of Runge-Kutta methods," *BIT Numerical Mathematics*, Vol. 31, No. 3, 1991, pp. 482–528.

[34] Ruuth, S., "Global optimization of explicit strong-stability-preserving Runge-Kutta methods," *Mathematics of Computation*, Vol. 75, No. 253, 2006, pp. 183–207.

[35] Qiu, Z., Zhang, B., Liang, C., and Xu, M., "A high-order solver for simulating vortex-induced vibrations using the sliding-mesh spectral difference method and hybrid grids," *International Journal for Numerical Methods in Fluids*, Vol. 90, No. 4, 2019, pp. 171–194.